PERGAMON

International Journal of Heat and Mass Transfer 45 (2002) 2315–2328

International Journal of HEAT and MASS TRANSFER

www.elsevier.com/locate/ijhmt

LES analysis of turbulent flow and heat transfer in motored engines with various SGS models

Horng-Wen Wu *, Shiang-Wuu Perng

Department of Naval Architecture and Marine Engineering, National Cheng Kung university, Tainan, Taiwan, ROC

Received 10 April 2001; received in revised form 12 October 2001

Abstract

This paper presents the application of three different subgrid-scale (SGS) models in a large eddy simulation (LES) for investigating the turbulent flow field and wall heat transfer during the compression–expansion strokes in two types of engine configuration under realistic engine conditions. Predictions were compared with experimental measurements (including the local heat flux and swirl velocity), and with those calculated from the conventional K–ε model. The results of the Van Driest wall damping model for LES were found to be in the best agreement with experimental data. The variations of velocity vector plots, isothermal profiles with crank angle were realized in the "Pancake" chamber engine. The variation of squish strength in the cylinder was also investigated by illustrating the friction velocity variations at different radial locations in the "Deep Bowl Piston" engine.

1. Introduction

Accurate, time-dependent, spatially resolved predictions of flow field and heat transfer will be of great assistance in the design of internal combustion engines. As has been certified by many investigators who have studied this problem, thermal efficiency, combustion, emissions, and structural integrity of an engine depend in some way upon the heat transfer from the confined gas to the combustion chamber surfaces in an engine [1]. Besides, the fluid flow plays an important role in fuel–air mixing, wall heat transfer and generation of turbulence, and exerts great influence on engine performance [2].

The purpose of this paper is to seek an appropriate turbulence model for predicting the fluid flow and wall heat transfer in the internal combustion engines. Although there have been many studies on the predictions of air motion and wall heat transfer with numerical methods [3,4], the most codes employ the Reynolds-averaged turbulence modeling (as the K–ε model) to simulate turbulent flow. The Reynolds-averaged simulations require a fine grid to resolve the regions of rapid variations. Given the complexity of the Reynolds-averaged simulations, the large eddy simulation (LES) might actually be simpler, shorter in execution and more accurate. In the Reynolds-averaged simulations the length scales of the turbulence usually are larger than the grid spacing. The Reynolds-averaged simulations only reveal unsteady motions of scales larger than the model's turbulence scale. Besides, the eddy viscosity is obtained from the length scale of the smallest eddy in the turbulence models. Therefore, the volume-averaged filtered Navier–Stokes equations are fairly insensitive to the turbulence models in the LES [5].

In this paper, the SIMPLE-C method [6] and LES [7] are employed in investigating the fluid flow and wall heat transfer in internal combustion engines. Second-order backward Euler (SBE) method [8] is implemented for discretizing the transient term to remove stability restrictions and extended linear upwind differencing (ELUD) method [9] (third-order scheme) for discretizing the convection terms to avoid severe oscillations. Also, iterative solution methods based on the preconditioned conjugate gradient method [10,11] were incorporated

* Corresponding author. Tel.: +86-6-274-7018; fax: +86-6-274-7019.

E-mail address: z7708033@email.ncku.edu.tw (H.-W. Wu).

0017-9310/02/$ - see front matter
PII: S0017-9310(01)00325-8

Nomenclature

A_{ij}, B_{ij}	terms for the dynamic model
$C_{\mathrm{I}}, C_{\mathrm{SD}}$	dynamic SGS model coefficient in the dynamic model
C_{K}	SGS model variable in LES ($C_{\mathrm{K}} = 0.094$)
C_{S}	Smagorinsky constant ($C_{\mathrm{S}} = 0.1$)
CR	compression ratio
D	bowl diameter
d	distance normal to a wall
d'	geometric length of an engine combustion chamber (including engine bore and distance from cylinder head to piston
E	empirical coefficient used for the wall function ($E = 9.0$)
E_{SGS}	subgrid-scale kinetic energy
f_μ	Van Driest wall damping function ($([1 - \exp(-Y^+/25)^3]^{1/2})$
G	grid filter function
(H)	the maximum value of the swirl velocity profile in the cylinder
h	enthalpy
L	characteristic length scale
(L)	the minimum value of the swirl velocity profile in the cylinder
N_{rpm}	engine speed
n	time level
P	pressure
P^*	summation of $\tilde{P}$ and $(2/3)E_{\mathrm{SGS}}$
Pr	Prandtl number
Pr_{T}	turbulent Prandtl number
q_{W}	wall heat flux
R	computational domain
S	modified factor of temperature boundary layer model
S^+	dimensionless modified factor ($S^+ \equiv S_v/q_{\mathrm{W}}U^*$)
S_{ij}	strain rate tensor of the flow field ($S_{ij} = (1/2)(\partial u_i/\partial x_j + \partial u_j/\partial x_i)$)
S_Φ	source term for variable
SR	initial swirl ratio ((initial swirl velocity)/$(2\pi r \times N_{\mathrm{rpm}})$)
SR_m	volume-averaged swirl ratio
t	time
T	temperature
T^+	dimensionless temperature ($T^+ \equiv \overline{\rho}C_{\mathrm{P}}\ (\tilde{T} - T_{\mathrm{W}})U^*/q_{\mathrm{W}}$)
T_{W}	wall temperature
TDC	top dead center
u_r, u_z, u_θ	velocity components along r, z, and θ axes
$\tilde{U}$	filtered velocity component parallel to the wall
U^*	friction velocity ($U^* \equiv \sqrt{\tau_{\mathrm{W}}/\overline{\rho}}$)
U^+	dimensionless velocity ($U^+ \equiv \tilde{U}/U^*$)
$\vec{V}$	velocity vector
x_i	cylindrical coordinates ($i = 1$ for radial coordinate r; $i = 2$ for axial coordinate z; $i = 3$ for azimuth coordinate θ)
y	near-wall distance
Y^+	dimensionless distance from the wall ($Y^+ \equiv yU^*/v$)

Greek symbols

α	constant equal to 0.2
$\overline{\Delta}$	grid filter width
$\hat{\Delta}$	test filter width
Φ	general dependent flow variable
Φ'	subgrid-scale component of Φ
Φ''	fluctuating quantity of Φ
κ	Von Karman constant
Γ_Φ	diffusion coefficient
μ_{lam}	laminar dynamic viscosity
μ_{T}	turbulent dynamic viscosity
μ_{eff}	effective dynamic viscosity
v	laminar kinematic viscosity
v_{T}	eddy viscosity
ρ	density
Ω	angular momentum of the whole swirl about the cylinder axis
Ω_0	initial value of Ω
Ω^*	ratio of Ω to Ω_0
τ_{W}	wall shear stress
θ	crank angle (degrees)
ξ	natural coordinate in computational domain

Superscripts

–	spatial grid filter indication
$\sim$	Favre-filtered indication
$\wedge$	test filter indication
$\langle\ \rangle$	volume-averaged indication

Subscripts

i, j	indication of components
r, z, θ	indication of cylindrical coordinate components

into the solving process with second-order time advancement. For mesh generation, the time-independent grid system [12] is used for constructing a local computational region attached to the moving boundary (moving piston) and faster convergence, and besides it generally requires less computer storage and computational time than the conventional method with the single-grid system at various crank angles.

In the first part of this paper, three different subgrid-scale (SGS) turbulence models for LES are compared with the experimental results [13] and the conventional K–ε model [3] on the local heat flux to verify their applicability in the "Pancake" chamber engine. Besides, we investigate the variations of flow field and temperature profile in the Pancake chamber engine; the interrelation between the flow field and temperature profile during the compression–expansion strokes is also observed. In the second part of this paper, the SGS models for LES are compared with the measured data [14] and the conventional K–ε model [4] on the swirl velocity to ensure the accuracy of these models applied in the "Deep Bowl Piston" engine. The three SGS models used in this paper are as follows: the modified Smagorinsky model, the Van Driest wall damping model [15], and the dynamic model [16]. In the Deep Bowl Piston engine, we investigate the fluid motion, the swirl–squish interactions, and the decay of swirl in the combustion chamber through the compression–expansion strokes. The results of this paper may be of interest to engineers attempting to develop a more suitable turbulence model for simulating turbulent flows in the complex geometries and to researchers interested in flow-modification aspects of fuel–air mixing and heat transfer in the combustion chamber.

2. Mathematical formulation

The thermal flow to be simulated is an unsteady, axisymmetric, compressible and viscous flow with turbulence by the LES using various SGS models. Calculation of the reciprocating thermal flow field in an engine requires obtaining the solution of the governing equations.

In LES the flow variables are decomposed into a large-scale component, denoted by an overbar, and a subgrid-scale component. The large-scale component is defined by the filtering operation

$$\overline{\Phi}(x_i,t)=\int_R G(x_i-\xi)\Phi(\xi)\,\mathrm{d}\xi,\quad \Phi=\overline{\Phi}+\Phi', \tag{1}$$

where the integral is extended over the entire domain R and G is the grid filter function. The length associated with G is the grid filter width $\overline{\Delta}$. For compressible flow, utilizing the Favre-filtered (or density-weighted) operation to treat the flow variables is necessary and then the variables is decomposed as follows:

$$\tilde{\Phi}=\frac{\overline{\rho\Phi}}{\overline{\rho}},\quad \Phi=\tilde{\Phi}+\Phi''. \tag{2}$$

The transport equations representing the conservation of mass, momentum and thermal energy are cast into a general form of time-dependent and axisymmetric cylindrical coordinates, and the governing transport equations filtered by a simple volume-averaged box filter are

$$\frac{\partial(\overline{\rho}\tilde{\Phi})}{\partial t}+\frac{1}{r}\left[\frac{\partial}{\partial z}\left(\overline{\rho}\tilde{u}_z r\tilde{\Phi}\right)+\frac{\partial}{\partial r}\left(\overline{\rho}\tilde{u}_r r\tilde{\Phi}\right)\right]=\frac{1}{r}\left[\frac{\partial}{\partial z}\left(r\Gamma_\Phi\frac{\partial\tilde{\Phi}}{\partial z}\right)+\frac{\partial}{\partial r}\left(r\Gamma_\Phi\frac{\partial\tilde{\Phi}}{\partial r}\right)\right]+S_\Phi(z,r), \tag{3}$$

where $\tilde{\Phi}$ represents one of the following entities: 1, $\tilde{u}_r$, $\tilde{u}_z$, $\tilde{u}_\theta$, or $\tilde{h}$, in which the dependent variables are radial velocity u_r, axial velocity u_z, swirl velocity u_θ, and enthalpy h. Also, t is time, ρ denotes density, and Γ_Φ and S_Φ stand for the corresponding effective diffusion and source term, respectively. The corresponding expressions of Γ_Φ and S_Φ are given in Table 1. In Eq. (3), the notation $\tilde{\Phi}=1$ denotes the continuity equation.

In Table 1, μ_{lam} is the laminar dynamic viscosity and calculated by the Sutherland law, μ_{eff} is the effective dynamic viscosity, P is pressure, T is temperature, E_{SGS} is subgrid-scale kinetic energy, and C_{P} is the specific heat at constant pressure. Assume the fluid to be an ideal gas with constant C_{P}, and then simplifying the energy equation by neglecting internal heat generation, radiation heat flux, and energy source [17].

2.1. Turbulence modeling

The conventional Smagorinsky SGS model [18] is used to obtain the eddy viscosity as follows:

$$\nu_{\mathrm{T}}=L^2\times\sqrt{2\times\tilde{S}_{ij}\tilde{S}_{ij}},\quad L=C_{\mathrm{S}}\times\overline{\Delta}, \tag{4}$$

where L is a characteristic length scale of small eddies, C_{S} is Smagorinsky constant ($C_{\mathrm{S}}=0.1$), $\overline{\Delta}$ is the grid filter width ($\overline{\Delta}=(\Delta r\Delta z)^{1/2}$) and $\tilde{S}_{ij}$ is a strain rate tensor of the filtered flow field:

$$\tilde{S}_{ij}=\frac{1}{2}\left(\frac{\partial\tilde{u}_i}{\partial x_j}+\frac{\partial\tilde{u}_j}{\partial x_i}\right),\quad |\tilde{S}|=\left(2\times\tilde{S}_{ij}\tilde{S}_{ij}\right)^{0.5}. \tag{5}$$

During initial runs of the present research, we discovered that the conventional Smagorinsky model did not generate appropriate levels of eddy viscosity in the complex physical domain. For the reason, the various SGS models are used here and described, respectively, as follows.

2.1.1. Modified Smagorinsky SGS model

In this model similar to Baldwin–Lomax model [19], the turbulent Prandtl number Pr_{T} is equal to 0.9 [20]. Besides, the eddy viscosity ν_{T} and the SGS kinetic energy E_{SGS} are obtained from the equations as follows:

$$\begin{aligned}&\nu_{\mathrm{T}}=L^2\times\sqrt{2\times\tilde{S}_{ij}\tilde{S}_{ij}},\\&L=\min\left(C_{\mathrm{S}}\times\overline{\Delta},\kappa d,\alpha d'\right),\quad E_{\mathrm{SGS}}=\overline{\rho}\left(\frac{\nu_{\mathrm{T}}}{C_{\mathrm{K}}\overline{\Delta}}\right)^2,\end{aligned} \tag{6}$$

where κ is Von Karman constant, α is equal to 0.2, C_{S} is equal to 0.1, C_{K} is equal to 0.094 [21], d is the distance

Table 1
Definition of $\tilde{\Phi}, \Gamma_\Phi$ and S_Φ

$\tilde{\Phi}$	Γ_Φ	S_Φ
1	0	0
$\tilde{u}_r$	μ_{eff}	$-\frac{\partial P^*}{\partial r}+\frac{\partial}{\partial z}\left(\mu_{\text{eff}}\frac{\partial \tilde{u}_z}{\partial r}\right)+\frac{\partial}{r\partial r}\left(r\mu_{\text{eff}}\frac{\partial \tilde{u}_r}{\partial r}\right)+\frac{\overline{\rho}\tilde{u}_\theta^2}{r}-2\frac{\mu_{\text{eff}}\tilde{u}_r}{r^2}-\frac{2}{3}\frac{\partial}{\partial r}\left(\mu_{\text{eff}}\nabla\cdot\vec{\tilde{V}}\right)$
$\tilde{u}_z$	μ_{eff}	$-\frac{\partial P^*}{\partial z}+\frac{\partial}{\partial z}\left(\mu_{\text{eff}}\frac{\partial \tilde{u}_z}{\partial z}\right)+\frac{\partial}{r\partial r}\left(r\mu_{\text{eff}}\frac{\partial \tilde{u}_r}{\partial z}\right)-\frac{2}{3}\frac{\partial}{\partial z}\left(\mu_{\text{eff}}\nabla\cdot\vec{\tilde{V}}\right)$
$\tilde{u}_\theta$	μ_{eff}	$-\overline{\rho}\frac{\tilde{u}_\theta\tilde{u}_r}{r}-\frac{\partial}{r\partial r}\left(r\mu_{\text{eff}}\frac{\tilde{u}_\theta}{r}\right)+\mu_{\text{eff}}\frac{\partial\left(\tilde{u}_\theta/r\right)}{\partial r}$
$\tilde{h}$	$\left(\frac{\mu}{Pr}\right)_{\text{eff}}$	$\frac{\mathrm{D}P^*}{\mathrm{D}t}+\mu_{\text{eff}}\left\{2\left[\left(\frac{\partial \tilde{u}_r}{\partial r}\right)^2+\left(\frac{\partial \tilde{u}_z}{\partial z}\right)^2+\left(\frac{\tilde{u}_r}{r}\right)^2\right]+\left(\frac{\partial \tilde{u}_r}{\partial z}+\frac{\partial \tilde{u}_z}{\partial r}\right)^2+\left(\frac{\partial \tilde{u}_\theta}{\partial z}\right)^2+\left[r\frac{\partial}{\partial r}\left(\frac{\tilde{u}_\theta}{r}\right)\right]^2-\frac{2}{3}\left(\nabla\cdot\vec{\tilde{V}}\right)^2\right\}$

Note:
$\mu_{\text{eff}}=\mu_{\text{lam}}+\mu_{\text{T}}, \quad \left(\frac{\mu}{Pr}\right)_{\text{eff}}=\left(\frac{\mu_{\text{lam}}}{Pr}\right)+\left(\frac{\mu_{\text{T}}}{Pr_{\text{T}}}\right), \quad h=C_{\text{P}}T, \quad P^*=\tilde{P}+\frac{2}{3}E_{\text{SGS}}, \quad \nu_{\text{T}}=\frac{\mu_{\text{T}}}{\overline{\rho}}.$

normal to a wall, and d' is the geometric length of an engine combustion chamber. The characteristic length scale was chosen as the minimum of all of the mixing lengths calculated to insure smooth transitions.

2.1.2. Van Driest wall damping SGS model

In this model, the turbulent Prandtl number Pr_{T} is still equal to 0.9. Also, the eddy viscosity ν_{T} and the SGS kinetic energy E_{SGS} are obtained from the equations as follows:

$$\begin{aligned}&\nu_{\text{T}}=L^2\times\sqrt{2\times\tilde{S}_{ij}\tilde{S}_{ij}}, \quad L=C_{\text{S}}f_\mu\overline{\Delta},\\ &E_{\text{SGS}}=\overline{\rho}\left(\frac{\nu_{\text{T}}}{C_{\text{K}}\overline{\Delta}}\right)^2,\end{aligned} \tag{7}$$

where C_{S} is equal to 0.15 [22], C_{K} is also equal to 0.094, and f_μ is the Van Driest wall damping function [15], $[1-\exp(-Y^+/25)^3]^{1/2}$, where $Y^+\equiv yU^*/\nu$. The Van Driest wall damping function is used to account for the near wall effect.

2.1.3. Dynamic SGS model

In dynamic SGS model, the model coefficients C_{SD} and C_{I} and the turbulent Prandtl number Pr_{T} are determined dynamically [16]. A "test filter" (denoted as $\wedge$) is introduced to derive an expression for C_{SD}, C_{I} and Pr_{T}. The key element of the dynamic model concept is the utilization of the spectral data contained in the resolved field. This information is brought to bear by introducing the test filter with a larger filter width than the resolved grid filter, which generates a second field with scales larger than the resolved field. The width of the test filter is taken to be twice the width of the grid filter. Therefore, the eddy viscosity ν_{T} and the SGS kinetic energy E_{SGS} are modeled from the equations as follows:

$$\begin{aligned}&\nu_{\text{T}}=L^2\times\sqrt{2\times\tilde{S}_{ij}\tilde{S}_{ij}}, \quad L^2=C_{\text{SD}}\overline{\Delta}^2,\\ &E_{\text{SGS}}=2C_{\text{I}}\overline{\rho}\overline{\Delta}^2|\tilde{S}|^2.\end{aligned} \tag{8}$$

In this model, C_{SD} and C_{I} are defined in Eq. (9) proposed by Germano et al. [16], and Pr_{T} is determined in Eq. (10) proposed by Moin et al. [23] as follows:

$$\begin{aligned}&C_{\text{SD}}=\frac{1}{2}\frac{\langle A_{ij}B_{ij}\rangle}{\langle B_{ij}B_{ij}\rangle}, \quad A_{ij}=\left(\widehat{\overline{\rho}\tilde{u}_i\tilde{u}_j}\right)-\frac{1}{\hat{\overline{\rho}}}\left(\widehat{\overline{\rho}\tilde{u}_i}\right)\left(\widehat{\overline{\rho}\tilde{u}_j}\right),\\ &B_{ij}=\overline{\Delta}^2\left(\widehat{\overline{\rho}|\tilde{S}|\tilde{S}_{ij}}\right)-\hat{\overline{\rho}}|\hat{\tilde{S}}|\hat{\Delta}^2\hat{\tilde{S}}_{ij},\\ &C_{\text{I}}=\frac{\left\langle\left(\widehat{\overline{\rho}\tilde{u}_i\tilde{u}_i}\right)-(1/\hat{\overline{\rho}})\left(\widehat{\overline{\rho}\tilde{u}_i}\right)\left(\widehat{\overline{\rho}\tilde{u}_i}\right)\right\rangle}{\left\langle 2\hat{\overline{\rho}}\hat{\Delta}^2\widehat{|\tilde{S}|^2}-2\overline{\Delta}^2\left(\widehat{\overline{\rho}|\tilde{S}|^2}\right)\right\rangle},\end{aligned} \tag{9}$$

$$Pr_{\mathrm{T}} = \frac{\left\langle C_{\mathrm{SD}}\left[\hat{\Delta}^2\hat{\overline{\rho}}|\widehat{\tilde{S}}|\frac{\widehat{\partial\tilde{T}}}{\partial x_i}\frac{\partial\tilde{T}}{\partial x_i} - \overline{\Delta}^2\left(\overline{\rho}|\tilde{S}|\widehat{\frac{\partial\tilde{T}}{\partial x_i}}\right)\frac{\partial\tilde{T}}{\partial x_i}\right]\right\rangle}{\left\langle\left[\frac{1}{\overline{\rho}}\left(\widehat{\overline{\rho}\tilde{u}_i}\right)\left(\widehat{\overline{\rho}\tilde{T}}\right) - \left(\widehat{\overline{\rho}\tilde{u}_i\tilde{T}}\right)\right]\frac{\partial\tilde{T}}{\partial x_i}\right\rangle}, \tag{10}$$

where $\hat{}$ is taken to indicate a test filter process, $\langle\ \rangle$ indicates volume averaged, and the width of test filter $\hat{\Delta}$ is twice the width of grid filter $\overline{\Delta}$.

2.2. Boundary conditions

Flow and temperature fields in the near-wall regions are matched to the boundary layer models. The modified wall function [24] is used to provide wall boundary conditions for velocity and temperature in the near-wall region.

In the laminar sublayer:

$$U^+ = Y^+, \tag{11}$$

$$T^+ = Pr\,Y^+ - 0.5\,Pr\,S^+(Y^+)^2, \quad Y^+ < 13.2. \tag{12}$$

In the turbulent boundary layer:

$$U^+ = \frac{1}{\kappa}\ln EY^+, \tag{13}$$

$$T^+ = 13.2\,Pr + 2.195\ln Y^+ - 5.66 - S^+(87.12\,Pr + 2.195Y^+ - 28.98), \quad Y^+ \geqslant 13.2. \tag{14}$$

Dimensionless variables with a superscript plus sign are defined as follows:

$$Y^+ \equiv \frac{yU^*}{v}, \quad U^+ \equiv \frac{\tilde{U}}{U^*}, \quad T^+ \equiv \frac{\overline{\rho}C_{\mathrm{P}}\left(\tilde{T} - T_{\mathrm{W}}\right)U^*}{q_{\mathrm{W}}}, \quad S^+ \equiv \frac{Sv}{q_{\mathrm{W}}U^*}. \tag{15}$$

The friction velocity U^* is defined as

$$U^* \equiv \sqrt{\frac{\tau_{\mathrm{W}}}{\overline{\rho}}}, \tag{16}$$

where v is the laminar kinematic viscosity, Pr is the Prandtl number, y is the distance from the wall, $\tilde{U}$ denotes the velocity component parallel to the wall, and S is the modified factor of the temperature boundary layer model as defined in Huh et al.'s study [24]. When $S = 0$, the model corresponds to the original logarithmic law of the wall.

No-slip boundary conditions are applied for velocities at all walls. At the piston crown, the axial velocity $\tilde{u}_z$ is assumed to equal the moving velocity of the piston. The wall temperature is assumed to be 350 K in the Pancake chamber engine and 320 K in the Deep Bowl Piston engine for simulating the case of a cold engine state.

2.3. Initial conditions

For the Pancake chamber engine, the calculations are started at a crank angle of 260° (100° BTDC (before top dead center)) in the compression stroke and terminated at 420° (60° ATDC (after top dead center)) in the expansion stroke for the engine speed of 1500 rpm. The initial air condition is assumed to be a solid-body rotation profile, $\tilde{u}_\theta(r) = 2\pi N_{\mathrm{rpm}}\mathrm{SR}r$, where N_{rpm} is the engine speed and SR (called the initial swirl ratio) is defined as the ratio of initial swirling speed (rpm) of the gas to engine speed. The initial swirl ratio equal to 3.37 was calculated from the phase-averaged LDV measured gas velocity data [13] at inlet valve closure (100° BTDC). The other two velocity components are induced by the piston motion and are much smaller than the azimuth component, so the axial velocity $\tilde{u}_z$ is assumed to vary linearly from cylinder head surface (zero velocity) to piston crown surface (moving boundary velocity). The radial velocity $\tilde{u}_r$ is assumed to be zero. The initial temperature is set equal to 350 K. For the Deep Bowl Piston engine, the calculations are started at a crank angle of 240° (120° BTDC) in the compression stroke and terminated at 390° (30° ATDC) in the expansion stroke for the engine speed of 900 rpm. According to the data utilized by Kondoh et al. [4], the initial conditions specified at the start of calculations, at 120° BTDC, are that the initial swirl ratio is 5.3, $\tilde{u}_z$ vary linearly from cylinder head surface to piston crown surface, $\tilde{u}_r$ is zero and the initial temperature is assumed to be 320 K.

3. Numerical method

Formulation and discretization of all transport equations are performed by using the SIMPLE-C algorithm with the control volume approach, with each equation arranged into transient, diffusion, convection, and source terms.

3.1. Convection term and time advancement

By adopting an ELUD [9] for discretizing the convective terms and a SBE [8] for discretizing the transient term, we may derive the fully discretized equations by means of control-volume method. These discretized equations are easily implemented into the SIMPLE-C algorithm.

3.2. Iterative method

The iterative solution methods based on the preconditioned conjugate gradient method are incorporated into this code. In this paper, the incomplete Cholesky conjugate gradient method (ICCG) [10] is used for the

Poisson pressure correction equation, and the incomplete LU Bi-conjugate gradient method (ILUBiCG) [11] is used for u_r, u_z, u_θ, h equations. The time step was tested to be set as 10^{-4} s for the calculations of unsteady flow and heat transfer in the cylinder chamber; we consider the difference in the calculated velocity fields and the mass residual as convergence conditions. The calculations were terminated when the mass residual is less than 10^{-4} and the relative error of velocity solution is less than 10^{-5}.

3.3. Grid generation approach

In this paper, the approach is used to treat the moving piston as a moving solid body in the computational domain without generating completely new grids at each time step. When the piston moves toward TDC or from TDC, the size of the domain will vary with the motion of the piston and those grids lying outside the body will be flagged as unused points that are excluded from the calculation. When the piston was moving away from TDC, it was necessary not only to interpolate the values back to their fixed grid locations but also to extrapolate the values of the time-dependent variables for two grid cells into the piston. This extrapolation was performed with a second-order Lagrange polynomial.

4. Results and discussion

A detailed numerical study has been carried out on two types of combustion chamber geometries used in the comparisons between the various turbulent SGS models for the LES. Two geometric sizes reflect the primary differences in geometric size between modern spark ignition engines and modern diesel engines. A schematic of two types of combustion chambers is shown in Fig. 1. Engine specifications are listed in Table 2.

4.1. Grid and time independence

In this paper, the grid and time step size sensitivity study was performed for the Pancake chamber engine with modified Smagorinsky SGS model to ensure that the results would not be influenced by inadequate discretization or too large a time step. This calculation was performed for a 2-D sector of the flow field with grid sets of mesh I [25 × 40 (for 100° BTDC)–25 × 6 (for TDC)], mesh II [32 × 50 (for 100° BTDC)–32 × 10 (for TDC)], mesh III [40 × 60 (for 100° BTDC)–40 × 14 (for TDC)], mesh IV [48 × 70 (for 100° BTDC)–48 × 18 (for TDC)], and mesh V [55 × 80 (for 100° BTDC)–55 × 22 (for TDC)]. Fig. 2(a) shows almost identical results for the calculated heat flux at the radial location of $r = 30.22$ mm on the cylinder head. Therefore, the grids

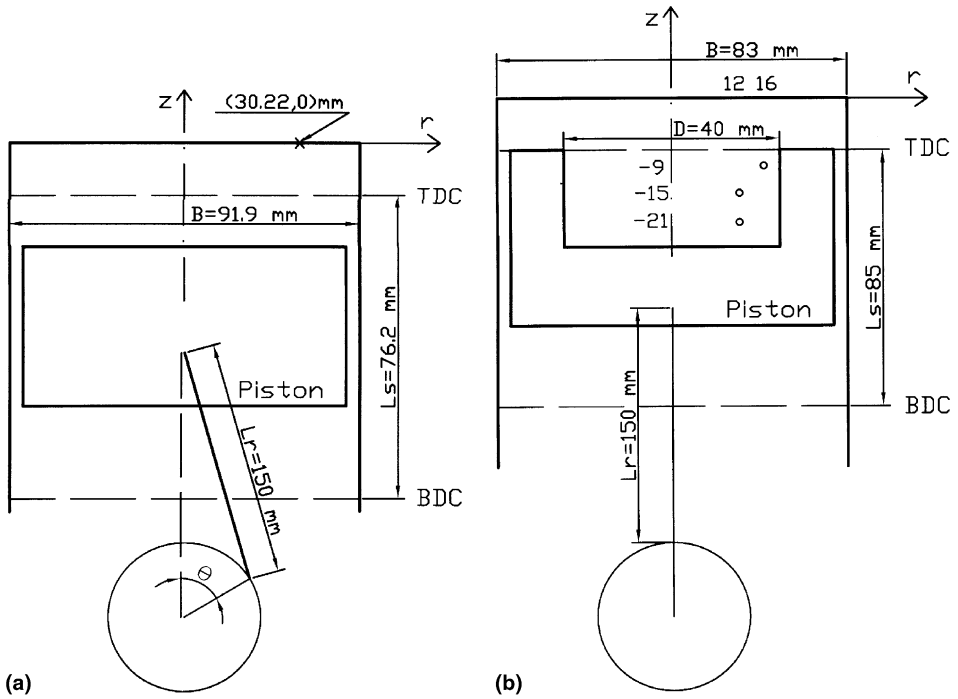

Fig. 1. Configurations and measured positions in different combustion chambers (a) "Pancake" chamber engine, (b) "Deep Bowl Piston" engine.

Table 2

"Pancake" chamber engine specifications	
Bore (mm)	91.9
Stroke (mm)	76.2
Displacement (cc)	505.4
Clearance volume (cc)	63.8
Initial swirl ratio	3.37
Compression ratio	8.92
Intake valve closes (starting time)	100° BTDC
Exhaust valve opens (finishing time)	60° ATDC
"Deep Bowl Piston" engine specifications	
Bore (mm)	83.0
Stroke (mm)	85.0
Displacement (cc)	460.0
Bowl diameter (mm)	40.0
Bowl depth (mm)	22.5
Clearance volume (cc)	47.75
Initial swirl ratio	5.30
Compression ratio	10.0
Starting time	120° BTDC
Finishing time	30° ATDC

as shown in Table 3 are used for all cases in this paper. The time step size is adjusted in this numerical code from stability and accuracy criteria with the initial time step size given as an input by the user. Three different time step sizes were chosen by limiting the maximum time step size at an engine speed of 1500 rpm. The three time steps in turn are 5×10^{-5}, 10^{-4}, and 2×10^{-4} s. According to the sensitivity results in Fig. 2(b), the heat flux curves tend to converge for the three time steps. The error is about 4–5% for the peak heat flux. Therefore, the time step 10^{-4} s is used for all the cases that follow in this paper.

4.2. Comparisons for the Pancake chamber engine

To show that the program of this paper handles turbulent heat transfer in the Pancake motored engine correctly, we apply the present numerical method with various turbulent SGS models to solve the unsteady heat transfer. Furthermore, the results of the local heat flux q_w ($r = 30.22$ mm as shown in Fig. 1(a)) are used to make a comparison between all cases including the various SGS models, the K–ε model predictions presented by Ikegami et al. [3], and the measurements conducted by Yang [13]. The heat flux comparisons as shown in Fig. 3 demonstrate that the K–ε model coupled the conventional wall function under-predicts the peak heat flux by about 30% from a comparison with the measurements. The three

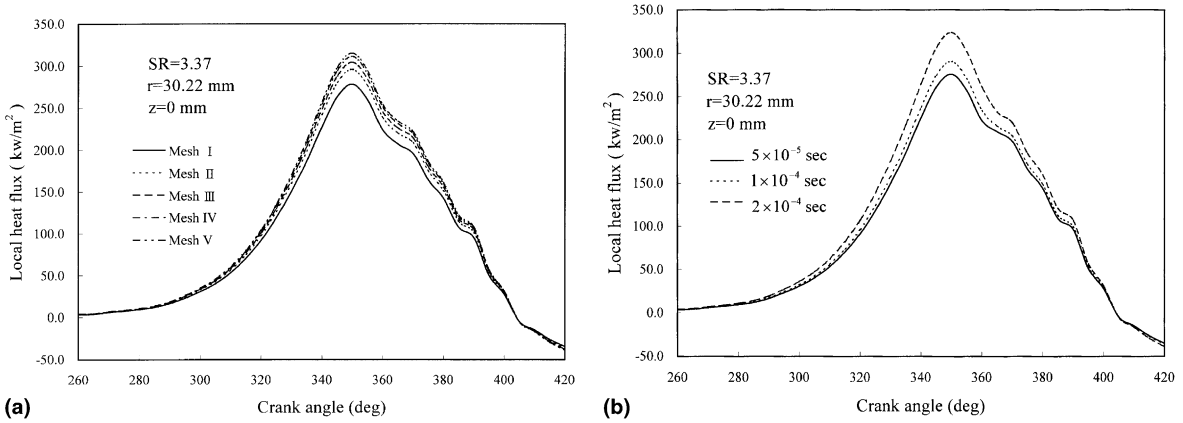

Fig. 2. (a) Grid sensitivity, (b) time step size sensitivity for the "Pancake" chamber engine motored at 1500 rpm.

Table 3
Computed cases for various engine geometries with different SGS models

Case	Combustion chamber	SGS model	Grid	CPU time
1	Pancake	Modified Smagorinsky model	32 × 50 (at 100° BTDC)	1 h 15 min 42 s
2		Van Driest wall damping model		1 h 27 min 11 s
3		Dynamic model		2 h 26 min 52 s
4	Deep Bowl Piston	Modified Smagorinsky model	32 × 64 (at 120° BTDC)	2 h 13 min 17 s
5		Van Driest wall damping model		2 h 22 min 39 s
6		Dynamic model		3 h 16 min 19 s

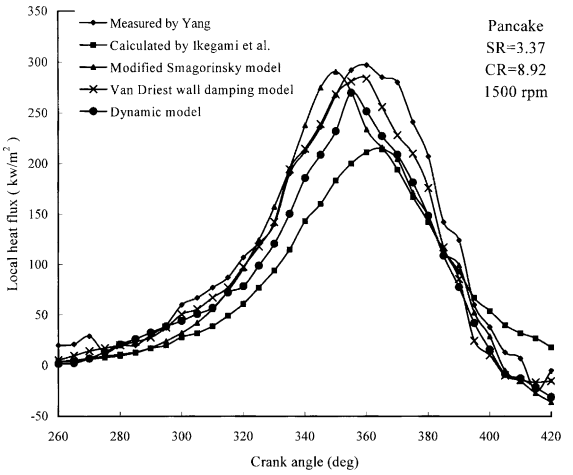

Fig. 3. Comparison of local heat flux between predictions and measurements for various crank angles in the "Pancake" chamber engine at 1500 rpm.

SGS models as shown in Table 3 of LES give better predictions for the peak heat flux that differ from the measurements by 2.6% using the modified Samgorinsky model, 4.7% using the Van Driest wall damping model, and 9% using the dynamic model. The modified Smagorinsky model has a phase difference from the measurements with the peak occurring at about 10° BTDC and has better predictions through the compression stroke than through the expansion stroke. The dynamic SGS model also has the appearance of the phase shift about 5° BTDC. The phase shift occurs due to the competing effects of the gas temperature which is the maximum at TDC and the rate-of-pressure rise term which is the maximum around 90° BTDC at the maximum piston speed and compression rate. Although the Van Driest wall damping model gives worse prediction for the peak heat flux than the modified Smagorinsky model, it makes the best prediction between three SGS models on the whole; especially, the prediction occurs at the period between 330° and 350°. Besides, the three models have the negative heat fluxes after about 45° ATDC due to the source term effect in the boundary layer.

In the numerical calculation of heat transfer, the key is not only the profile of the flow velocity but also that of the air temperature in the cylinder. The flow field development predicted by using the Van Driest wall damping SGS model in the Pancake chamber engine is shown at three different crank angles around TDC in Fig. 4. Two velocity components in the radial and axial direction are induced by the piston motion. Besides, the fluid for the Pancake chamber engine cannot produce squish motion, so there is no the squish flow in the cylinder. The "roll-up" vortex is seen at the corner between the piston and the cylinder wall (Fig. 4(a)); and the vortex is formed since the upward fluid flow hits the

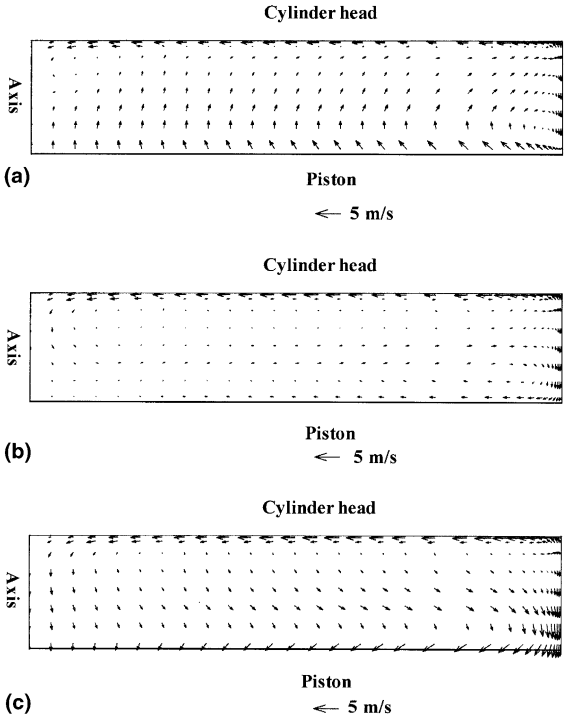

Fig. 4. Velocity vector plots on the axial–radial plane for crank angle equal to (a) 350° (10° BTDC), (b) 360° (TDC), (c) 370° (10° ATDC) in the "Pancake" chamber engine at 1500 rpm.

cylinder head. At TDC (Fig. 4(b)), the piston motion is stopped, so the flow velocity is weaker than that in Fig. 4(a). After the piston passes through TDC, the flow field

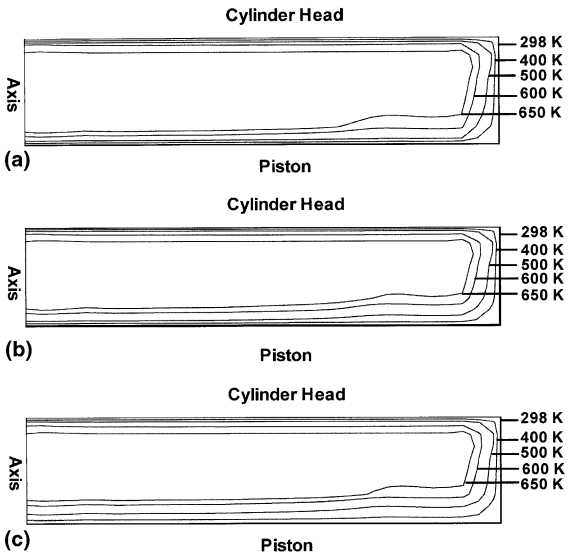

Fig. 5. Isothermal plots for crank angle equal to (a) 350° (10° BTDC), (b) 360° (TDC), (c) 370° (10° ATDC) at 1500 rpm in the "Pancake" chamber engine.

seems to form a counter-clockwise circulation in the cylinder owing to downward piston motion (Fig. 4(c)). Fig. 5 illustrates the isothermal distribution of three different crank angles as described in Fig. 4. Closer isothermal lines indicate a higher temperature gradient and accordingly a higher heat flux. From the isothermal plots in Fig. 5, the temperature gradient along the cylinder head surface is the maximum for three wall surfaces. This trend is caused by the stronger parallel velocity along the cylinder head surface (see Fig. 4). For cylinder head surface, the temperature gradient at TDC (Fig. 5(b)) is the largest between three different crank angles in Fig. 5; then the timing at TDC has the largest values of heat flux between three various crank angles in the Van Driest wall damping SGS model.

4.3. Comparisons for the Deep Bowl Piston engine

A Deep Bowl Piston engine was used to indicate that the present method is feasible for predicting the squish and swirl flow in the cylinder. In this paper, we would take the results of the local swirl velocity $\tilde{u}_\theta$ (three "o" notations as shown in Fig. 1(b)) to compare with the measured data presented by Ohkubo et al. [14] and the numerical results calculated by Kondoh et al. [4]. Besides, we would use the results of the local swirl velocity to realize the difference between three SGS models in this type of combustion chamber. Fig. 6 presents the comparison on the time history of swirl velocity in the Deep Bowl Piston engine. Fig. 6(a) shows that the swirl velocity has a peak at about 355° for three SGS models

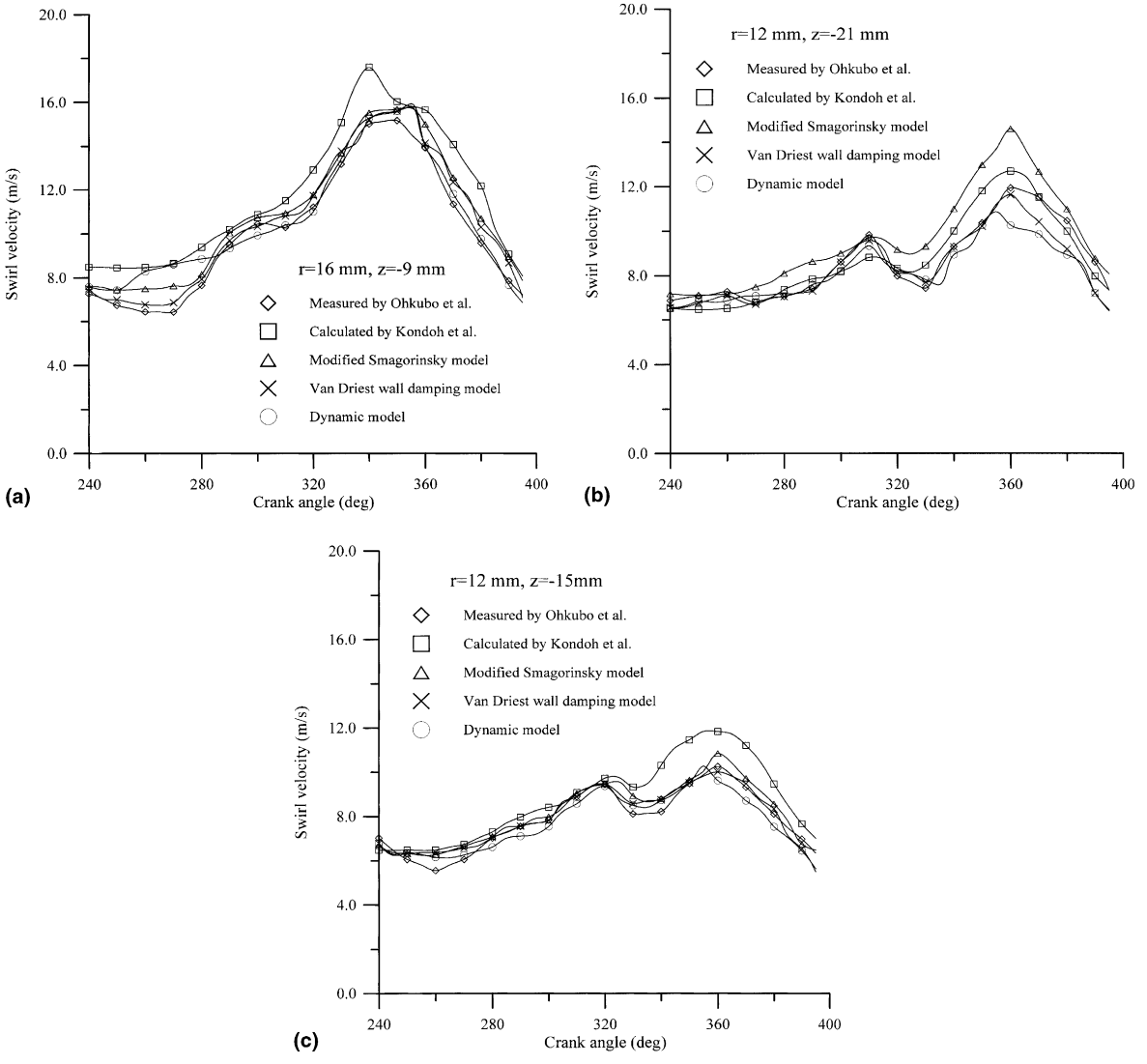

Fig. 6. Comparison of local swirl velocity on (a) $r = 16$ mm, $z = -9$ mm, (b) $r = 12$ mm, $z = -15$ mm, (c) $r = 12$ mm, $z = -21$ mm between predictions and measurements for various crank angles in the "Deep Bowl Piston" engine at 900 rpm.

in this paper. The peak timing obtained from this paper is closer to the measured peak timing than that from the numerical result predicted with the K–ε model adopted by Kondoh et al. Besides, the K–ε model under-predicts the swirl velocity by within 34% from a comparison with the measurements; three SGS models used in this paper give better predictions for the swirl velocity that differ from the measurements within 18% using the modified

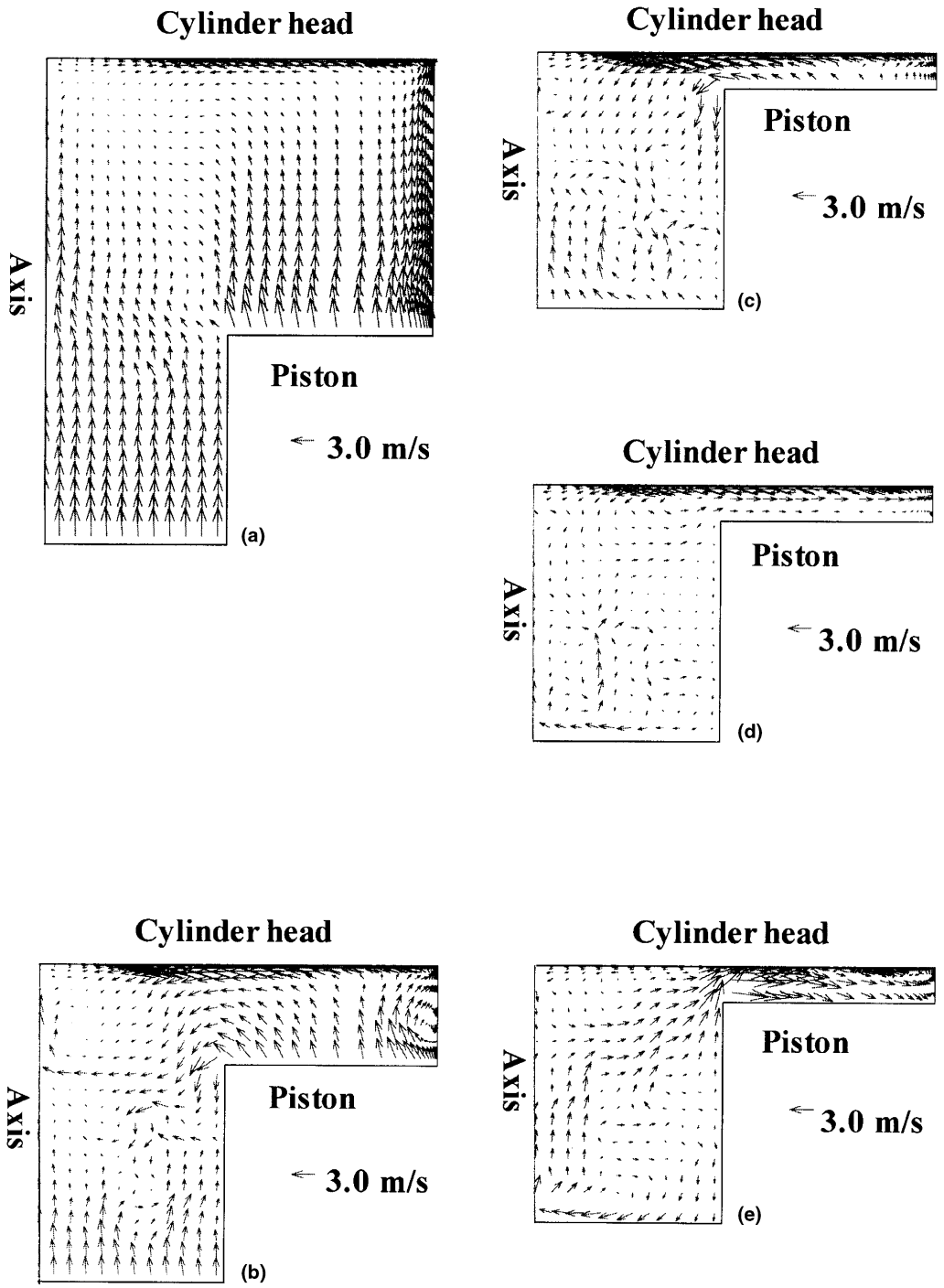

Fig. 7. Velocity vector plots on the axial–radial plane for crank angle equal to (a) 300° (60° BTDC), (b) 330° (30° BTDC), (c) 350° (10° BTDC), (d) 360° (TDC), (e) 370° (10° ATDC) in the "Deep Bowl Piston" engine at 900 rpm.

Smagorinsky model, 10% using the Van Driest wall damping model, and 27% using the dynamic model. In Figs. 6(b) and (c), the measured data revealed that the swirl velocity has another peak except the maximum value at TDC. This nature is very well reproduced by the calculation. The three SGS models used in this paper

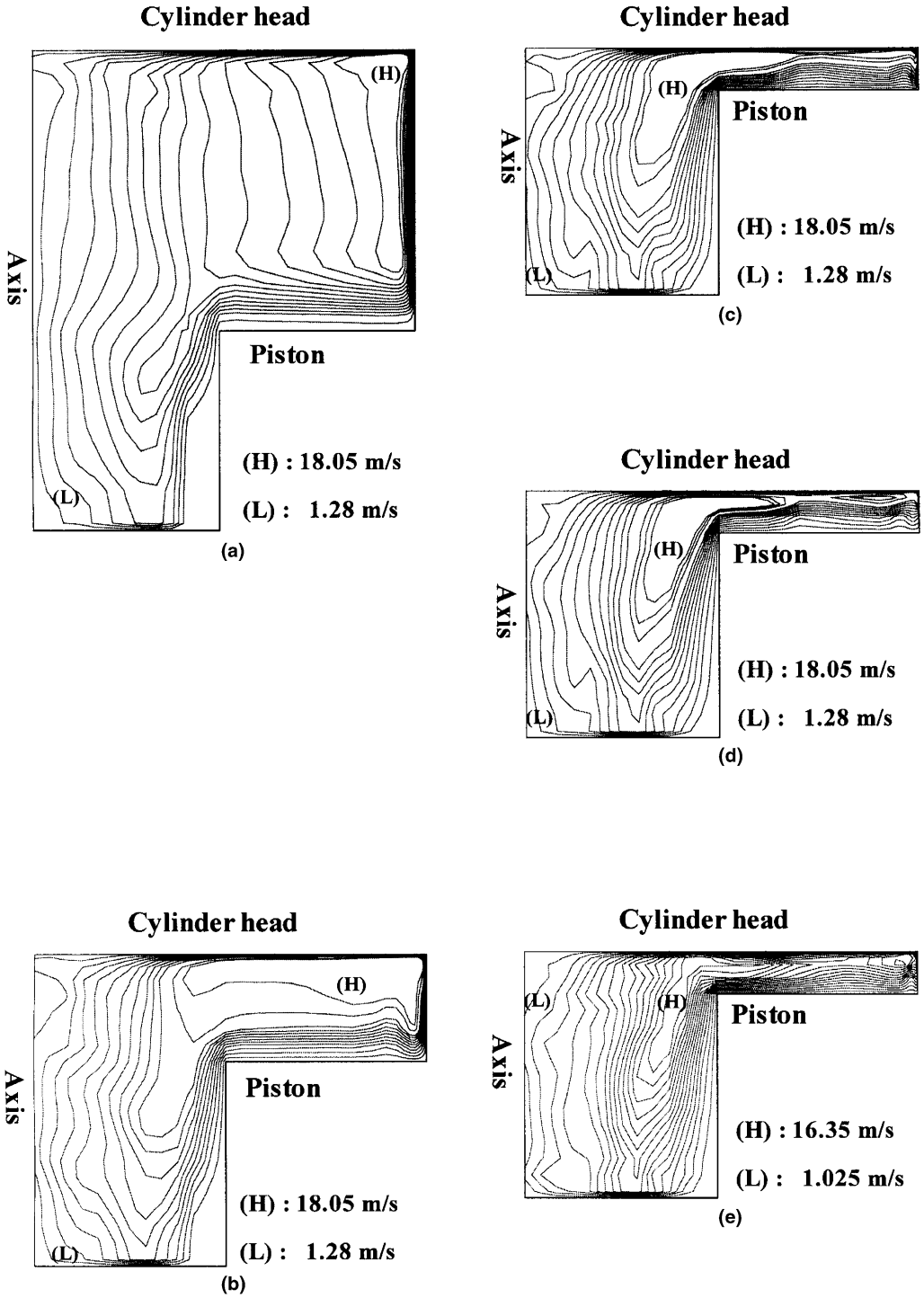

Fig. 8. Contour lines of swirl velocity for crank angle equal to (a) 300° (60° BTDC), (b) 330° (30° BTDC), (c) 350° (10° BTDC), (d) 360° (TDC), (e) 370° (10° ATDC) in the "Deep Bowl Piston" engine at 900 rpm.

predict the swirl velocity better than the K–ε model utilized by Kondoh et al. The advantage is obvious around TDC. On the whole, the Van Driest wall damping model has the best prediction for the swirl velocity between three SGS models and K–ε model.

Figs. 7 and 8 show the flow field development predicted by the Van Driest wall damping SGS model for the Deep Bowl Piston engine. It is seen that the flow field is dominated by the swirl and squish flow near TDC. At 10° BTDC (Fig. 7(c)), there is strong radial flow toward the axis (called "squish") above the piston head, which was caused by a large difference of compression between the inner (smaller radius) and the outer (bigger radius) region. There is a ring vortex with the clockwise rotation in the piston bowl. At TDC (Fig. 7(d)), the squish motion has mostly disappeared and there is another vortex with the counter-clockwise rotation around the top of the piston bowl. At 10° ATDC (Fig. 7(e)), there is strong radial flow toward the cylinder wall (called "reverse squish") above the piston head. Fig. 8 shows contour lines of the swirl velocity $\tilde{u}_\theta$ in the Deep Bowl Piston engine at various crank angles. The distribution of $\tilde{u}_\theta$ does not differ so much from that of the initial swirl profile until crank angle reaches about 300°. After that crank angle, as the angular momentum in the squish region is transferred into the piston bowl by the squish flow (see Fig. 8(b)), the position of the maximum value for $\tilde{u}_\theta$ moves into the piston bowl at 350° (see Fig. 8(c)). $\tilde{u}_\theta$ at TDC almost has the same distribution as that at 350° in the piston bowl. After TDC, the maximum value of $\tilde{u}_\theta$ decreases, but it occurs near the top edge of the piston bowl. In order to comprehend the squish effect on the flow field, we utilize Fig. 9 to investigate the variation of squish strength. The friction velocity variations at different radial locations as illustrated in Fig. 9 show

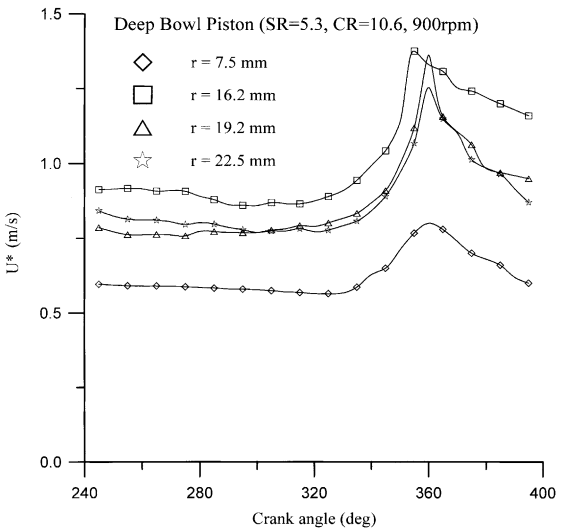

Fig. 9. Friction velocity variation of the "Deep Bowl Piston" engine at 900 rpm for four different radial locations on the cylinder head.

that the squish flow has the maximum effect near the top edge of the piston bowl and the maximum squish effect occurs between 10° BTDC and TDC. The flow field in the Deep Bowl Piston engine is characterized by high swirl and high squish as compared with that of the Pancake chamber engine.

4.4. Decay of swirl in the Deep Bowl Piston engine

Due to the importance of the swirl flow in the combustion chamber, we investigate the variations of Ω (angular momentum of the whole swirl about the cyl-

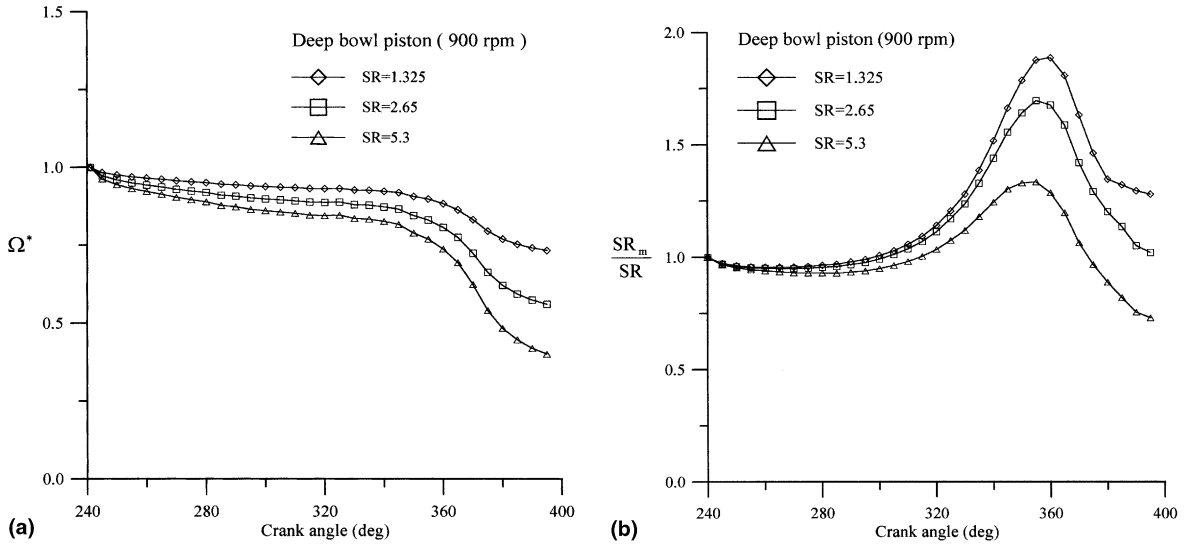

Fig. 10. Effects of initial swirl ratio on (a) Ω^*; (b)$\mathrm{SR}_m/\mathrm{SR}$ in the "Deep Bowl Piston" engine at 900 rpm.

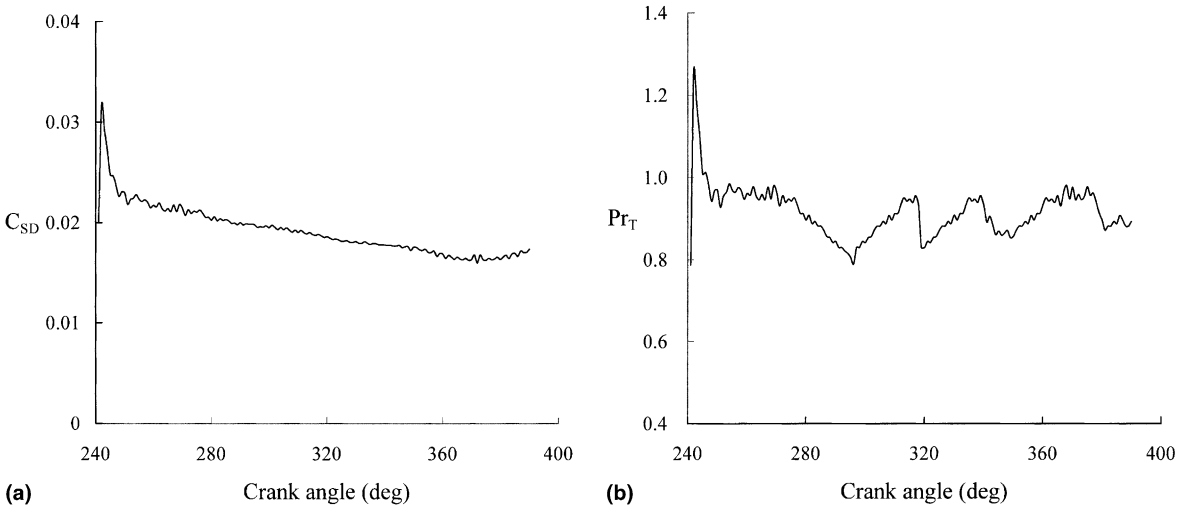

Fig. 11. Time history of the dynamic SGS model coefficients (a)C_{SD}, (b) Pr_T for the "Deep Bowl Piston" engine at 900 rpm.

inder axis) and SR_m (volume-averaged swirl ratio) at different crank angles. Shown in Fig. 10 are the variations of the ratio $\Omega^* = \Omega/\Omega_0$ and SR_m/SR with various crank angles in the Deep Bowl Piston engine under the conditions that the initial swirl ratio SR is equal to 1.325, 2.65 and 5.3 at an engine speed of 900 rpm. Fig. 10(a) presents that the amount of the decay of Ω^* becomes large with an increase in SR (similar tendency is found in [25]). The maximum value of SR_m/SR at $SR = 1.325$ occurs at TDC, and the peak value is decreasing and the peak timing is shifting to 5° BTDC with an increase in initial swirl ratio SR as shown in Fig. 10(b). The decrease of Ω^* is presumably due to the relative decrease in the effect of wall friction in the squish area, for the angular momentum in the squish region is transferred into the bowl by the squish flow as described in Figs. 7 and 8. Then, the bigger amount of decay of swirl represents that the maximum value of swirl velocity is transferred into the bowl, which is effective in promoting the mixing of fuel and air.

4.5. Comparisons between three SGS models

From the above discussions about the numerical predictions for Pancake and Deep Bowl Piston engines in this paper, we find that the Van Driest wall damping SGS model predicts the local heat flux and swirl velocity better than the other two models except for the peak heat flux. Although the model coefficient C_{SD}, C_I and Pr_T of the dynamic SGS model are not set to be constant and obtained through the test filter process, the dynamic SGS model does not seem to predict better than the other two models under the axisymmetric hypothesis. Besides, the dynamic model costs CPU time (executed in Pentium II 300 PC) more than the other two SGS models about 1 h. This is due to the various model coefficients. Furthermore, we plot the dynamic model coefficients history as shown in Fig. 11. The coefficients are fluctuating at beginning and then keep in the region around the values of 0.02 (C_{SD}) and 0.93 (Pr_T). The value of 0.02 obtained from the dynamic model is between 0.01 (C_S^2 for the modified Smagorinsky model) and 0.0225 (C_S^2 for the Van Driest wall damping model), and the value of 0.93 is near the value of 0.9 (Pr_T for the other two models).

5. Conclusions

Three subgrid-scale (SGS) models of LES, including the modified Smagorinsky model, the Van Driest wall damping model, and the dynamic model, were implemented for predicting the flow field and wall heat transfer in two types of engine configuration. On the basis of these results presented and discussed in Section 4, we draw the main conclusions below:

- Overall results were comparable with those of the conventional K–ε turbulence model; on the whole, the three SGS models of LES with modified wall function method give better predictions for the local heat flux and swirl velocity than the K–ε model in two types of engine configuration.
- From among three SGS models, the Van Driest wall damping SGS model makes the best prediction for the local heat flux and swirl velocity except the peak heat flux in two various engine geometries, and it costs CPU time less than the dynamic SGS model.
- In the "Pancake" chamber engine, the maximum heat flux occurs at TDC for the Van Driest wall damping SGS model; the peak timing is the same as the measured result.

- In the "Deep Bowl Piston" engine, the squish flow has the maximum effect near the top edge of the piston bowl and this effect occurs between 10° BTDC and TDC; hence, there is a ring vortex with the clockwise rotation in the piston bowl.
- With increasing the initial swirl ratio, the amount of decay of Ω^* increases while the maximum value of SR_m/SR decreases. The bigger amount of decay of swirl is promoting the mixing of fuel and air more effectively.
- Interaction between piston motion, induced squish and swirl motion has great influences on determining the unsteady flow fields.

Acknowledgements

The authors gratefully acknowledge the partially financial support of this project by the National Council of the Republic of China.

References

[1] G. Borman, K. Nishiwaki, Internal combustion engine heat transfer, Prog. Energy Combust. Sci. 13 (1) (1987) 1–46.
[2] A.D. Gosman, R.J.R. Johns, Development of a predictive tool for in-cylinder gas motion in engines, SAE 780315, 1978.
[3] M. Ikegami, Y. Kidoguchi, K. Nishiwaki, A multidimensional prediction of heat transfer in non-fired engines, SAE 860467, 1986.
[4] T. Kondoh, A. Fukumoto, K. Ohsawa, Y. Ohkubo, An assessment of a multi-dimensional numerical method to predict the flow in internal combustion engines, SAE 850500, 1986.
[5] C. Fureby, G. Tabor, H.G. Weller, A.D. Gosman, A comparative study of subgrid scale models in homogeneous isotropic turbulence, Phys. Fluids 9 (5) (1997) 1416–1429.
[6] G. Raithby, I. Van Doormaal, Enhancements of the SIMPLE method for predicting incompressible fluid flows, Numer. Heat Transfer 7 (1984) 147–163.
[7] B. Galperin, S. Orszag, in: Large Eddy Simulation of Complex Engineering and Geophysical Flows, Cambridge University Press, Cambridge, 1993, pp. 231–346.
[8] G.B. Deng, J. Piquet, P. Queutey, M. Visonneau, A new fully coupled solution of the Navier Stokes equations, Int. J. Numer. Methods Fluids 19 (1994) 605–639.
[9] Y.Y. Tsui, A study of upstream weighted high-order differencing for approximation to flow convection, Int. J. Numer. Methods Fluids 13 (1991) 167–199.
[10] D. Kershaw, The incomplete Cholesky-conjugate gradient method for the iterative solution of systems of linear equations, J. Comp. Phys. 26 (1978) 43–65.
[11] H. Van Der Vorst, BI-CGSTAB: a fast and smoothly converging variant of BI-CG for the solution of nonsymmetric linear system, SIAM J. Sci. Stat. Comput. 13 (2) (1992) 631–644.
[12] J.Y. Tu, L. Fuchs, Overlapping grids and multigrid methods for three-dimensional unsteady flow calculation in IC engines, Int. J. Numer. Methods Fluids 15 (1992) 693–714.
[13] J. Yang, Convective heat transfer predictions and experiments in an IC Engine, Ph.D. Thesis, University of Wisconsin–Madison, 1988.
[14] Y. Ohkubo, M. Ohtsuka, J. Kato, K. Kozuka, K. Sugiyama, Study of the in-cylinder flow (Part 1: Swirl velocity measurements by back-scattered LDV), in: 4th Joint Symposium on Internal Combustion Engines, 1984, pp. 31–36 (in Japanese).
[15] U. Piomelli, High Reynolds number calculations using the dynamic subgrid scale stress model, Phys. Fluids A 5 (6) (1993) 1484–1490.
[16] M. Germano, U. Piomelli, P. Moin, W. Cabot, A dynamic subgrid-scale eddy viscosity model, Summer Program, Center for Turbulence Research, Stanford University, Stanford, CA, 1990.
[17] J.R. Smith, An accurate Navier–Stokes solver with an application to unsteady flows, Ph.D. Thesis, West Virginia University, Morgantown West Virginia, 1996.
[18] J. Smagorinsky, General circulation experiments with the primitive equations, I. The basic experiment, Mon. Weather Rev. 91 (3) (1963) 99–164.
[19] D. Wilcox, in: Turbulence Modeling in CFD, second ed., DCW Industries, Inc, Glendale, CA, 1993, pp. 52–53.
[20] A.W. Verman, B.J. Geurts, J.G.M. Kuerten, P.J. Zandbergen, A finite volume approach to large eddy simulation of compressible, homogeneous, isotropic, decaying turbulence, Int. J. Numer. Methods Fluids 15 (1992) 799–816.
[21] A. Yoshizawa, K. Horiuti, Statistically-derived subgrid-scale kinetic energy model for the large-eddy simulation of turbulent flows, J. Phys. Soc. Jpn. 54 (8) (1985) 2834–2839.
[22] S. Sakamoto, S. Murakami, A. Mochida, Numerical study on flow past 2D square cylinder by large eddy simulation: comparison between 2D and 3D computations, J. Wind Eng. Ind. Aerodyn. 50 (1993) 61–68.
[23] P. Moin, K. Squires, W. Cabot, S. Lee, A dynamic subgrid-scale model for compressible turbulence and scalar transport, Phys. Fluids A 3 (11) (1991) 2746–2757.
[24] K.Y. Huh, I.-P. Chang, J.K. Martin, A comparison of boundary layer treatments for heat transfer in IC engines, SAE 900252, 1990.
[25] T.W. Kuo, V.K. Duggal, Modeling of in-cylinder flow characteristics – effect of engine design parameters, in: T. Uzkan (Ed.), Flows in Internal Combustion Engines – II, ASME, New York, 1984, pp. 9–17.